3D-Printed Strain Sensors: Electro-Mechanical Simulation and Design Analysis Using Nonlinear Material Model and Experimental Investigation

S. M. Mahdi Mofidian, Shayan Davani, Kasra Momeni, and Hamzeh Bardaweel

***Abstract*—This work is driven by the continuous improvement in additive manufacturing and the growing interest in developing flexible strain sensors with complex designs and structures. Characterization and analysis require not only understanding the mechanical behavior of the sensor but also the electrical behavior and the coupled electromechanical behavior. Traditionally, this coupled electromechanical behavior is determined using simplified approaches to establish a relationship between the electrical domain and mechanical domain. This work presents an experimental and numerical platform to characterize strain sensors and serves as a tool for design guidelines for these sensors. A nonlinear finite element COMSOL model is developed and validated against experiment. At 38% strain level the sensitivity is increased by 7% when the thickness,t, of the sensor decreased from t = 1.4 mm to t = 0.6 mm. A sensor with triangular embedded channels exhibits improved performance compared to square, hexagonal, and octagonal cross-sectional shapes. Three common channel patterns are examined including spiral, vertical serpentine, and horizontal serpentine patterns. Three commonly used materials for fabricating strain sensors are investigated including PDMS, EcoFlex, and NinjaFlex. At 35% strain level, a sensor with NinjaFlex substrate exhibits, approximately, 6% improvement in sensitivity, compared to a sensor with EcoFlex substrate.**

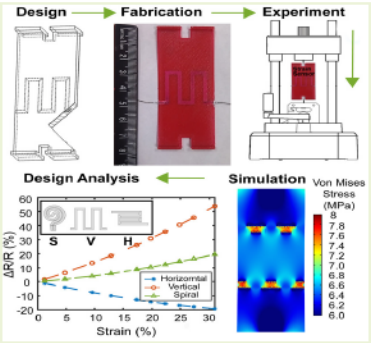

***Index Terms*—Flexible strain sensor, 3D printed sensor, finite element modeling, hyper-elastic material, liquid metal sensor.**

I. Introduction

ADVANCED manufacturing techniques have led to a growing interest in the fabrication of flexible sensors. Among those devices are strain sensors that can be used in a variety of applications, including robotics, prosthetics, automobile industry, and machine environment interphases [1]–[15]. Chief among strain sensors is the resistive-type strain sensor, shown in Fig. 1. The sensor uses a flexible substrate coupled with an electric conductor to allow for a change in electric resistance as a result of mechanical deformation in the flexible substrate [16].

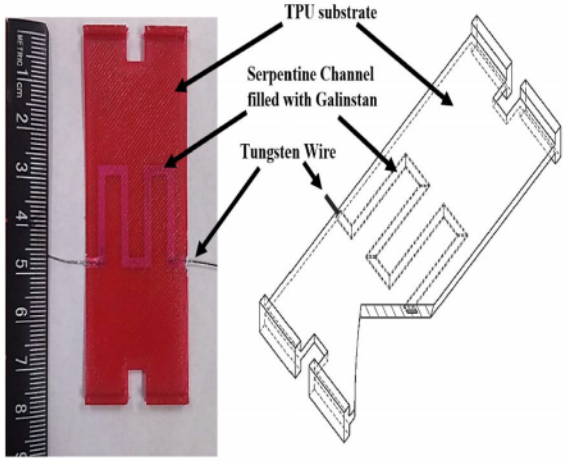

Fig. 1. A representative resistive-type strain sensor structure consists of a flexible substrate, fluid passages (embedded micro-channels), and liquid metal conductor.

Typical conductors used in these sensors include liquid metals, conductive polymers, and conductive inks. PDMS and other rubber-like materials such as EcoFlex and NinjaFlex

Manuscript received August 11, 2020; revised August 30, 2020; accepted August 30, 2020. Date of publication September 3, 2020; date of current version December 16, 2020. This work was supported in part by DoE-ARPA-E OPEN under Grant DE-AR0001066, in part by NASA-EPSCoR, in part by Louisiana Tech University, and in part by NSF-CAREER under NSF cooperative agreement under Grant CBET-1943857. The associate editor coordinating the review of this article and approving it for publication was Prof. Weileun Fang. *(S. M. Mahdi Mofidian and Shayan Davani contributed equally to this work.) (Corresponding author: Hamzeh Bardaweel.)*

S. M. Mahdi Mofidian, Shayan Davani, and Hamzeh Bardaweel are with the Mechanical Engineering Department, College of Engineering and Science, Louisiana Tech University, Ruston, LA 71270 USA, and also with the Institute for Micromanufacturing, College of Engineering and Science, Louisiana Tech University, Ruston, LA 71270 USA (e-mail: hamzehb@latech.edu).

Kasra Momeni is with the Department of Mechanical Engineering, University of Alabama, Tuscaloosa, AL 35487 USA.

This article has supplementary downloadable material available at https://ieeexplore.ieee.org, provided by the authors.

Digital Object Identifier 10.1109/JSEN.2020.3021576

are among the most common materials used to fabricate these strain sensors [16]. Over the past few years, several fabrication techniques have been used to fabricate these strain sensors [4], [17].

Molding, lithography, planar printing, coating, and additive manufacturing are among the most common fabrication methods used to manufacture these sensors [4], [18]–[21]. For instance, Case *et al.* [22]. utilized the soft lithography method using a Universal Laser Systems to fabricate a dog-bone shaped resistive strain gauge sensor for application in the soft robotic industry. Additive manufacturing provides a cost-effective, efficient, and highly versatile approach to fabricating flexible strain sensors. Furthermore, additive manufacturing is attractive because it facilitates the construction of complex designs and geometries, allows rapid design iterations with minimum wasted material, does not require cleanroom environments, does not require advanced and costly labor training [10], [23]. To this end, several researchers have successfully demonstrated the use of additive manufacturing to fabricate flexible sensors [4], [10], [11], [17], [24]. For example, Muth *et al.* [4] used a modified inkjet printer to fabricate flexible strain sensors by embedding a conductive ink into an elastomer. Similarly, Agarwala used inkjet printing to fabricate micro-channels in a composite rubber substrate with 500 μm diameter channels [10]. Smith *et al.* fabricated a uniaxial strain sensor using commercially available NinjaFlex Thermoplastic Polyurethane (TPU) flexible polymer and desktop Fused Deposition Modeling (FDM) 3D printing to obtain embedded micro-channels that were then filled with liquid metal conductor [16].

The previous discussion reveals that there are both increasing interest and an urgent need for flexible sensors. To this end, the main objective of this work is performing numerical studies to understand, analyze, and characterize the performance and response of these strain sensors. The numerical platform developed in this work serves as a tool for the design strategies and guidelines of these strain sensors. The presented work is driven by the continuous improvement in additive manufacturing technologies as well as soft and flexible materials that open the gate for fabricating sensors with more elaborate designs and structures. These sensors represent coupled electromechanical systems. Thus, full characterization, design, and analysis require not only understanding the mechanical behavior of the sensor but also the electrical behavior and the coupled electromechanical effect on the sensor response [25]. Traditionally, this coupled electromechanical behavior has been determined using simplified analytical formulas to establish a relationship between the electrical resistance change ΔR, and strain, ε such as those reported in [16], [19], [26], [27]. These traditional models do not consider the nonlinear behavior of the rubber-like materials used for these sensors, which results in a discrepancy between theoretical predictions and experimental data. Besides, in these theoretical approaches, owing to both geometrical and mathematical complexities, the relationship between electric domain, i.e., changes in electrical resistance, ΔR, and mechanical domain, i.e., mechanical strain, ε, does not take into account the interaction between embedded liquid metal channel and its substrate. Moreover, the deployment of a new generation of wearable sensors requires higher accuracy to monitor/record the data, leading to sensors with more complex geometries. For these reasons, there is an urgent need to develop a computational platform that serves as a tool to understand, analyze, and optimize the continuously advancing strain sensor structures. To the best knowledge of the authors, there are only a few studies that have numerically investigated these types of sensors. For example, Overvelde *et al.* [25]. developed a finite element-based model to simulate the mechanical and electrical performance of a liquid metal flexible sensor. They assumed a neo-Hookean material model for EcoFlex substrate with rectangular and semi-circular cross-sectional micro-channels and focused on different loading conditions.

In this work, we fabricate a prototype of a strain sensor and develop a coupled electro-mechanical finite element model using COMSOL software and use it to understand and analyze the characteristics of a resistive-type strain sensor. We also perform a comprehensive parametric study to investigate the critical geometrical/material characteristics and maximize the sensor's sensitivity. Here, we implement a nonlinear finite element technique with two parameters Mooney-Rivlin hyper-elastic material model and validate these simulations against experimental data. The work presented in this article provides a full insight into the effects of various design parameters and lays out strong design guidelines and roadmap for flexible strain sensors.

II. Methods

A. Experimental Procedure

1) Fabrication: Fig 1. shows a schematic of the resistive-type strain sensor used for model validation in this work. The main constituents of the strain sensor are U-shaped embedded channels, conductive fluid, and substrate material. The U-shaped channel consists of long and short channels that altogether make a flexible conductive path. External loading results in the deformation of the cross-sectional area and elongation of these channels. Therefore, leading to a change in electrical resistance of the conductive fluid inside these channels. The amount of strain experienced by the sensor can be estimated by tracking changes in the electric resistance. The U-shaped channels are embedded inside a substrate and obtained via additive manufacturing. First, we prepared a 3D CAD sketch of the sensor using SolidWorks software, which was then used to create the correspondingly STL file that is compatible with 3D printer software Cura. Upon fabrication, the Ultimaker 3 FDM 3D printer was used to obtain the substrate of the sensor. Commercial 3D materials of NinjaFlex Thermoplastic Polyurethane (TPU) (Shore hardness 85A) and Polyvinyl Acetate (PVA) were used to obtain the substrate and support materials, respectively. The role of the support material, i.e. PVA, was to prevent the channel from being filled or clogged by the substrate material during the 3D printing process. Later these channels were filled with a conductive fluid material. Once the 3D printing process was complete, the PVA support material was removed using boiling water and a 0.16 gauge tungsten wires were inserted into the ports on both sides of the channel as connecting wires and

TABLE I
SPECIFICATIONS AND PRINTING CONDITIONS USED TO 3D PRINT THE STRAIN SENSOR FOR MODEL VALIDATION PURPOSES

Thermoplastic Polyurethane (TPU)	
Flow (%)	106
Generate Support	on
Horizontal Expansion (mm)	0.16
Infill Density (%)	100
Infill Pattern	Grid
Layer Height (mm)	0.04
Line Width (mm)	0.35
Printing Temperature (°C)	245
Speed (mm/s)	20
Poly Vinyl Acetate (PVA)	
Flow (%)	100
Horizontal Expansion (mm)	0.16
Infill Density (%)	100
Infill Pattern	Grid
Layer Height (mm)	0.04
Line Width (mm)	0.35
Printing Temperature (°C)	215
Speed (mm/s)	80

sealed using liquid rubber sealant. After the rubber seal dried, the fabricated channel was filled with the conductive fluid, Galinstan (Ga 68.5% In 21.5% Sn 10%, Rotometals). In the process of filling the channel, the air removal and injection of the Galinstan was done, simultaneously, to prevent bubbles from forming inside the channel. For this purpose, one needle was utilized to inject Galinstan in one side and a second needle was used to remove air from the other side of the channel. The detailed schematic of the fabrication process is presented in a previous work of the authors [16]. Also, the channel was checked for any defects or holes using confocal laser scanning microscope (VK-100X) to make sure that there is no leakage [16]. Settings and conditions used for 3D printing the substrate are presented in Table I.

2) Experiment Setup: The experiment setup shown in Fig. 2 was utilized in testing and characterizing the fabricated strain sensor. In the setup, the test bench (PASCO ME-8236 Materials Testing Machine) with a built-in optical encoder module and load cell capable to measure up to 7100 N were used to measure the displacement and axial force, respectively. The test bench machine transfers the data through Bluetooth connection (PASCO airlink PS-3200) to a PC for later analysis. Tungsten wires in both sides of the strain sensor were connected to a data acquisition system (DAQ). Additionally, a circuit was utilized to measure the change of resistance in the strain sensor. For this purpose, a constant voltage of 5V was running across a 120Ω resistor that was connected in series with the strain sensor. The electric circuit was utilized to increase the accuracy of measured resistance change because the resistance of the strain sensor was relatively small. The strain sensor was latched into a pair of aluminum mounts from the bottom and fixed to the force cell by a hook from the top. A hand-wheel was used to manually crank two lead-screws in both sides of the machine causing the vertical movement of the

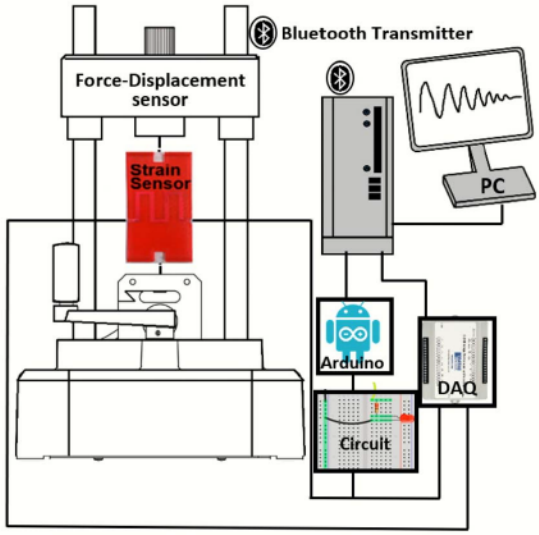

Fig. 2. Experiment setup used in this work to characterize the resistive-type strain sensor.

force bar. The sensor was stretched/un-stretched as the force bar was moving. This change in length of the sensor when subject to the external loading, Δl, causes the strain in the sensor, defined as $\varepsilon = \Delta l / l_0$ where l_0 represents the original length of the sensor. Due to this strain, the cross-sectional area and, consequently, the resistance across the strain sensor, ΔR, change. The change in resistance across the strain sensor was measured as voltage drop across external load resistance.

B. Numerical Method

Fig. 3 shows a flowchart describing the finite element model structured inside COMSOL software. A 3-D stationary model of the strain sensors was developed and implemented using commercial finite element-based software, COMSOL Multiphysics®. For this purpose, referring to Fig. 3, the geometry of the strain sensor was generated using SolidWorks CAD software and then imported into COMSOL software. During the simulation process, a coupled multi-physics model of the electric and mechanical domains of the strain sensor was created using conjugated structural mechanics and AC/DC modules. In the structural mechanics module, a hyper-elastic Mooney-Rivlin model for the TPU substrate was implemented in order to accurately predict the behavior of the substrate material. The coefficients of this model were calculated using least squares method fitted to the measured experimental data. Next, all the needed material properties for both the substrate and liquid conductive metal were imported into COMSOL. Then, the boundary conditions were defined for the structure. Here, an interactive boundary condition between the channel wall and the conductive liquid metal was constructed to accurately represent the multi-physics of the structure. In this boundary condition it was assumed that the deformation of the channel, because of the strain force, leads to volume change of the channel. The volume change affects the internal pressure of the conductive liquid metal and, consequently, the liquid metal resists the exerted compression and tends to rebuild the pressure inside

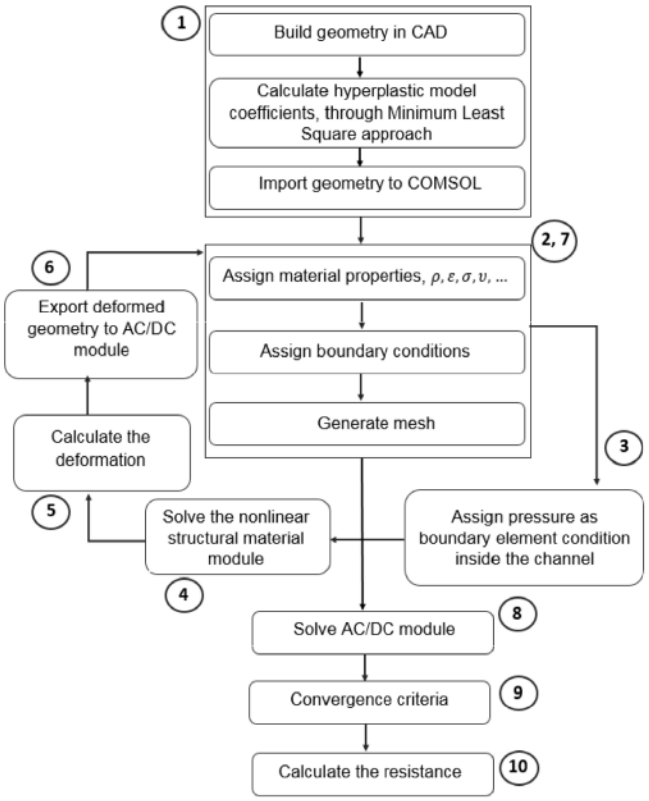

Fig. 3. Flowchart of steps taken to obtain the coupled finite element model of the strain sensor.

the channel. In the following step, the substrate deformation at different strains was solved continuously in COMSOL structural mechanics module and the deformed geometry was exported into the AC/DC module to calculate the resistance change due to this deformation across the channel.

1) Constitutive Model of Substrate: The substrate of the sensor was fabricated using TPU; a rubber-like material. Rubber-like materials are characterized by large deformations, very large bulk modulus (almost incompressible), and nonlinear stress-strain (constitutive material model) relationships [28]. Moreover, its hyper-elastic behavior shows time and temperature dependency [29] with hysteresis and cyclic softening [30]. Boyce *et al.* used constitutive models to account for this behavior which was observed during uniaxial compression testing of the TPU [30]. They decomposed their constitutive model into a rate-independent and a rate-dependent terms. While the rate-independent term demonstrated a rubber-like hyper-elastic behavior, the rate-dependent term followed viscoelastic-plastic model characteristics. For small strain levels, the TPU substrate shows a fairly little hysteric behavior dictated by the small area enclosed inside the stress-strain curve [16]. Moreover, recent studies have shown that if the rate-dependent term is negligible, incompressible hyper-elastic material models such as Odgen and Mooney-Rivilin are capable of satisfactorily predicting the behavior of the TPU [29]. For instance, Reppel and Weinberg [31] used various hyper-elastic models such as neo-Hookean, Mooney-Rivilin (two parameters), and Odgen models to describe the behavior of these rubber-like materials. Their Mooney-Rivilin model showed an excellent prediction of the material behavior up to 200% strain. Therefore, in this study and for simplicity, the viscoelastic behavior of the TPU substrate was neglected for the stationary analysis and Mooney-Rivlin model was adopted. A uniaxial tensile test was performed, and measured stress-strain data was used to obtain the Mooney-Rivlin model coefficients using optimization module in COMSOL.

2) Hyper-Elastic Model: For the rubber-like substrate, the strain energy function W_s, is defined in terms of principal strain invariants of either left or right Cauchy-Green deformation tensors, $\boldsymbol{B} = \boldsymbol{F}\boldsymbol{F}^T$ [32] and given by:

$$I_1 = \mathrm{tr}(\boldsymbol{B}) = \lambda_1^2 + \lambda_2^2 + \lambda_3^2 \tag{1}$$

$$I_2 = 1/2\left(\{\mathrm{tr}(\boldsymbol{B})\}^2 - \mathrm{tr}(\boldsymbol{B}^2)\right) = \lambda_1^2\lambda_2^2 + \lambda_2^2\lambda_3^2 + \lambda_1^2\lambda_3^2 \tag{2}$$

$$I_3 = \det(\boldsymbol{B}) = \lambda_1^2\lambda_2^2\lambda_3^2 \tag{3}$$

where $\boldsymbol{B}$ is the deformation, I_i are the principal strain invariants, and λ_i, the stretch ratios, are square root of the eigenvalues of $\boldsymbol{B}$. For an isotropic material stretched in one direction ($\lambda_2 = \lambda_3$) and considering the incompressibility ($I_3 = 1$) dictated by large bulk modulus κ, the deformation gradient $\boldsymbol{B}$ can be expressed as:

$$\boldsymbol{B} = \begin{bmatrix} \lambda_1^2 & 0 & 0 \\ 0 & \lambda_1^{-1} & 0 \\ 0 & 0 & \lambda_1^{-1} \end{bmatrix} \tag{4}$$

The nominal engineering stress (first Piola-Kirchoff stress), $\boldsymbol{P}$ is calculated from strain energy function, W_S, [27]:

$$P(\lambda) = 2\left(\lambda - \frac{1}{\lambda^2}\right)\left(\frac{\partial W_s}{\partial I_1} + \frac{\partial W_s}{\partial I_2}\frac{1}{\lambda}\right) \tag{5}$$

For general Mooney-Rivilin formulation, the strain energy function, W_s is given by:

$$W_s = \sum_{i=0,j=0}^{\infty} C_{ij}(I_1 - 3)^i + (I_2 - 3)^j \tag{6}$$

where $C_{00} = 0$, and the other coefficients depend on the material properties. For the two-parameter Mooney-Rivilin model used in this study, the truncated form of (6) is given by:

$$W_s = C_{10}(I_1 - 3) + C_{01}(I_2 - 3) \tag{7}$$

Substituting W_s in first Piola-Kirchoff stress, $\boldsymbol{P}$ yields:

$$P(\lambda) = 2\left(C_{10} + C_{01}/\lambda\right)\left(\lambda - 1/\lambda^2\right). \tag{8}$$

Here, Mooney-Rivilin coefficients C_{10} and C_{01} are calculated through fitting the experimental data of P_i (engineering stress measured during the uniaxial tensile test) versus λ (the stretch obtained from $\lambda = 1 + \varepsilon$) where ε is the engineering normal strain. Consequently, shear modulus, G for small strain can be valuated from the sum of these coefficients and given by [29]:

$$G = 2(C_{10} + C_{01}) \tag{9}$$

3) Structural Model: After determining material model for the TPU, the sensor's substrate geometry was meshed without meshing the liquid metal channel. In this work. the bulk modulus of liquid metal, i.e. eGaIn was considered to be $\kappa = 2$ GPa. To account for the impact of liquid metal on the structural behavior and, consequently, the electric resistance of

the sensor, an additional equation was solved, simultaneously, for calculating the internal pressure of the liquid metal:

$$V_{\text{deformed}} = V_{\text{initial}} \times (1 - P/k) \tag{10}$$

where V_{deformed}, V_{initial}, P, and κ are the deformed and undeformed volume of the liquid channel, internal pressure, and bulk modulus of the liquid metal, respectively. Equation (10) calculates the pressure in the liquid by assuming the volume of the liquid channel remains almost unchanged under different loadings or strains applied to the substrate. This is a reasonable assumption due to the nearly incompressible behavior of the liquid metal ($\kappa = 2$ GPa). V_{deformed} was calculated from the deformed surface of the liquid metal-channel walls, S_{deformed}, mutual with the interior boundary of the TPU substrate using divergence theorem principal given by:

$$V_{\text{deformed}} = \iiint_V (1)dV = \iiint_V \left(\nabla . \begin{bmatrix} x \\ 0 \\ 0 \end{bmatrix}\right) dV = \iint_{S_{\text{deformed}}} x n_s dS \tag{11}$$

where V is the volume, n_x is the x-component of the surface normal vector, and S is the boundary surface of V. In (10), P accounts only for the liquid pressure change due to the volume change of the liquid metal, and the hydrostatic pressure distribution exerted by gravity is neglected. This is because despite of the comparatively high density of the liquid metal, i.e. eGaIn (6.44 Kg/m^3), the volume of the channel is small (4.4 E-8 m^3) and the gravity force, and consequently hydrostatic pressure in the liquid metal, can be neglected. The calculated pressure P was directly applied as a load boundary condition on S_{deformed}.

After computing the substrate deformation at different strain levels, the deformed geometry was re-meshed and exported to another COMSOL component as a meshed geometry. Then, the internal volume of the liquid metal channel was isolated and defined as a new domain in the AC/DC module to find the electric resistance of the deformed channel. The electrical conductivity of the liquid metal, eGaIn, was assigned as 3.46E6 (S/m) [33]. In the AC/DC module, and in order to determine the resistance along the two sides of the liquid metal channel, one side was considered as the ground while the other side was connected to a terminal with constant current source of 1 A. In the meshing process, tetrahedral elements were used in both the substrate solid domain and the deformed liquid metal domain. Mesh independency was examined in structural mechanics module for the TPU domain, as well as the AC/DC module for the eGaIn domain. Consequently, the satisfactory levels of refinement without compromising the computation speed were 84000 and 3038 domain elements for the TPU and eGaIn domains, respectively.

III. Results and Discussion

A. Model Validation Using Experiment

Material properties of a 3D printed TPU substrate greatly depend on printing conditions [31]. Therefore, it is essential to examine the 3D printed TPU samples presented in this work experimentally in order to estimate the Mooney-Rivilin coefficients, i.e. C_{10} and C_{01}, of these samples. To this end, first, a strip of TPU was 3D printed using printing conditions shown in Table I. The experiment setup shown in Fig. 2 was then used to obtain stress-strain curves of the 3D printed TPU strips. The C_{10} and C_{01} coefficients corresponding to the minimum least squares error were evaluated −0.32832 (MPa) and 2.9437 (MPa), respectively. Fig. 4 examines the measured stress-strain curve and compares it with the stress-strain curve reported by Reppel and Weinberg [31]. Results reveal that the 3D printed TPU substrates presented in this work demonstrate similar trends and characteristics compared to those reported by Reppel and Weinberg [31]. The deviation between the stress-strain curves measured in this work and reported by Reppel and Weinberg is likely due to variation in printing conditions.

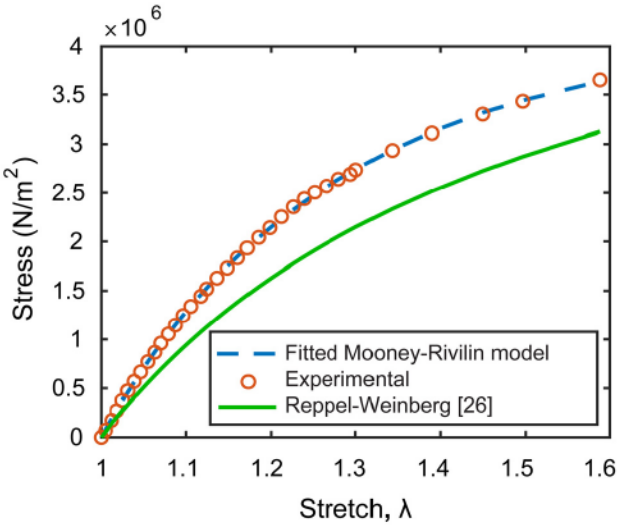

Fig. 4. Measured stress-strain curve of the 3D printed TPU substrates presented in this work, Mooney-Rivilin model, and measured stress-strain curve of 3D printed TPU substrates reported by Reppel-Weinberg [31].

Next, the numerical simulation results were validated against the experimentally measured data. Here, model simulations of both electric resistance and displacement versus loading are compared against measured data. For this purpose, first, using the experimental setup shown in Fig. 2, a uniaxial force was applied across the sensor. The applied force was gradually increased to 50 N. Simultaneously, the elongation due to the exerted force was measured using the displacement sensor. Results from the experiment and model simulation are shown in Fig. 5a. Next, changes in electric resistance, ΔR, were measured, and the nominal engineering strain, ε, was calculated using the measured elongation from the sensor along the loading direction. Fig. 5b shows the normalized measured changes in electric resistance, ΔR/R versus nominal strain, ε. The gauge factor parameter, GF $= \Delta$R/($\varepsilon \cdot$ R), of the sensor at different strain levels is discussed in a previous work of the authors [16]. Fig. 5b also compares the numerical simulations obtained using the Mooney-Rivlin hyper-elastic model against the measured data. Results from Fig. 5(a-b) demonstrate an excellent agreement between model simulations and measured data. Results also show that nonlinear effects become evident at higher strain levels. Thus, the nonlinear model developed in

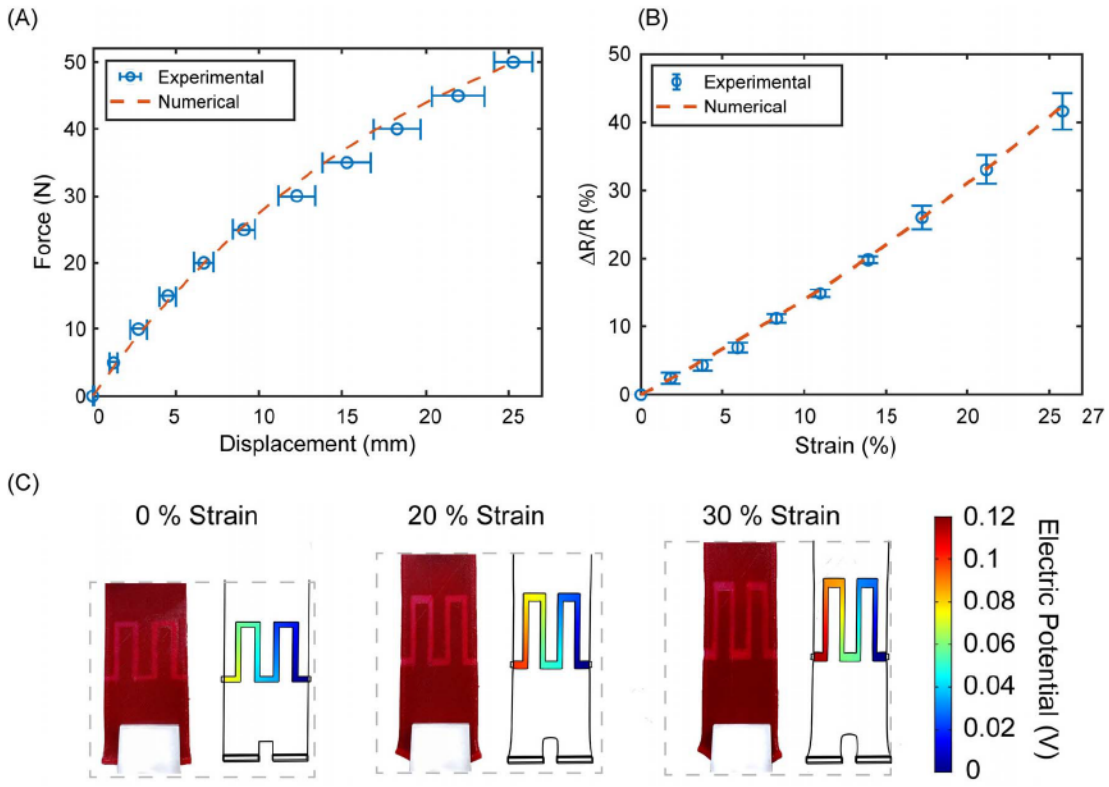

Fig. 5. Comparison between numerical simulations and experimental data: a) Displacement versus force, b) Electric resistance change versus strain, and c) Deformation at different strain levels.

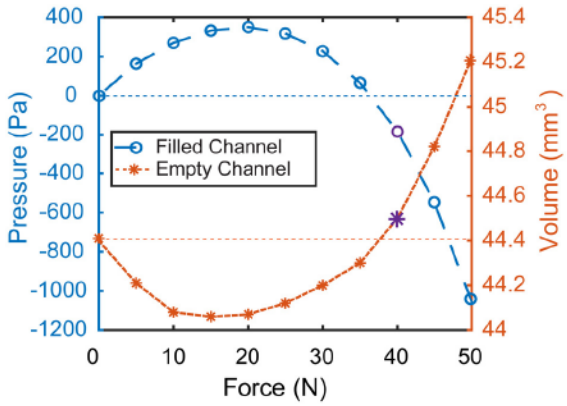

Fig. 6. Internal pressure in the filled channel of the sensor and volume of an empty channel as functions of uniaxial loading force.

this work is essential to capture the nonlinear behavior of the strain sensor. Unlike commonly used linear simplified models, the nonlinear model developed in this work can accurately predict the response of the sensor over a wider range of strain levels because of the nonlinear hyper-elastic model that is coupled with the electrical-mechanical solver. The error bar of the experimental data was calculated from three sets of experiments. The resemblance between the sensor deformation predicted by the model simulations and experimental data at 0%, 20%, and 30% strain levels is shown in Fig. 5c.

The internal pressure of the liquid metal filling the U-shaped embedded channel of the sensor is shown in Fig. 6.

Interestingly, instead of a monotonously increasing, the pressure increases to its peak at 20 N force and then decreases gradually to reach negative values at applied forces above the 35 N. This behavior can be explained better in light of volume change of the channel.

That is, to further investigate the relation between the pressure and the volume, a sensor with an empty channel was analyzed under the same loading boundary conditions. Results of volume changes of the empty channel versus applied force are shown in Fig. 6.

As it can be seen, the negative values of pressure occur close to the points where the volume of the empty channel surpasses its unstrained value. For better demonstration, the first data points, below the blue dashed line for filled channel and above the orange dashed line for empty channel, are marked with a different color (purple). Also, the extremums of the two curves occur at a comparatively close applied force (maximum occurs around 20 N for the filled channel compared to the minimum occurs around 15 N for the empty channel curve).

B. Design Study and Optimization

In this section, we investigate the effect of critical design parameters in order to establish design guidelines for improving the performance of the strain sensor. Specifically, we use the numerical platform developed and validated in previous sections to study the effect of substrate thickness, substrate material, channel aspect ratio, channel geometry, and channel location and pattern on the performance of the strain sensor. In these simulations, nominal parameters shown in Table II were fixed, and only the design parameter under investigation was altered. The volume of the liquid sensor was kept constant, while other parameters were altered.

TABLE II
NOMINAL DIMENSIONS OF THE 3D PRINTED STRAIN SENSOR PRESENTED IN THIS WORK

Parameter	Dimension (mm)
Thickness of the sensor	0.6
Length of the sensor	80
Width of the sensor	31
Thickness of the channel	0.1
Length of the channel	111
Width of the channel	2

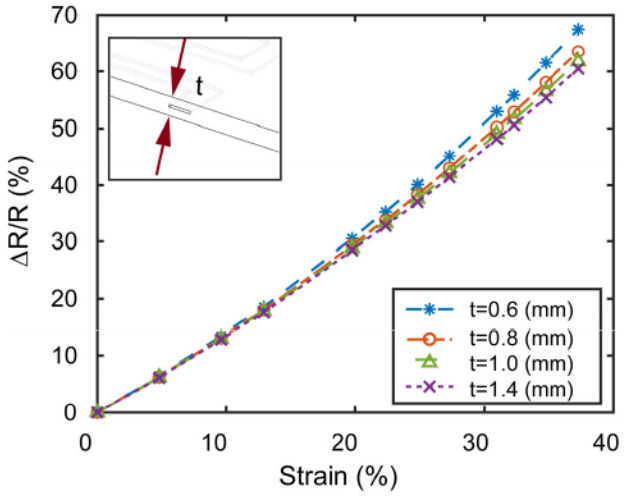

Fig. 7. Effect of thickness of the substrate on the sensitivity of the strain sensor.

1) Substrate Thickness: Fig. 7 investigates the effect of the thickness of the substrate on the sensitivity of the strain sensor. Here, the sensitivity of the sensor is expressed in terms of the relative change in electric resistance in response to given strain, i.e., $\Delta R/R$.

As shown in Fig. 7, the sensitivity of the strain sensor slightly improves as its thickness decreases. For instance, the change in the electric resistance, $\Delta R/R$ at 38% strain is increased by 7% when the thickness of the sensor, t, decreased from $t = 1.4$ mm to $t = 0.6$ mm.

This increase in sensitivity is expected because the loading force which is transmitted to the boundaries of the channel depends on the thickness of the substrate. Thus, a thinner substrate is more susceptible to deformation. Additionally, the loading force required to stretch the sensor to the same strain level depends on the thickness of the substrate. This is further investigated in Fig. 8, where von Mises stress distributions in the sensor at different external force levels are obtained using model simulations. Here, the boundary condition applied for both substrates is fixed at 35% strain level. For this strain level, the force, and consequently the stress, in the thinner substrate is smaller, as shown in Fig. 8.

2) Microchannel Width: The effect of the aspect ratio (AR = width of the channel/height of the channel) of therectangular embedded channels on the performance of the strain sensor is shown in Fig. 9. Due to the limited thickness of the substrate, only the AR ≥ 1 is considered in this study.

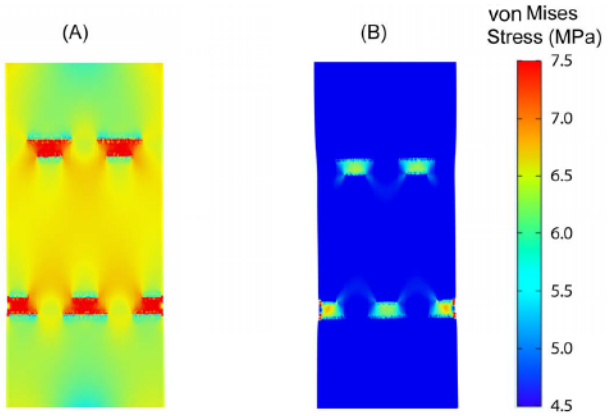

Fig. 8. von Mises stress distributions in the strain sensor: a) 1.4 mm thick substrate and b) 0.6 mm thick substrate.

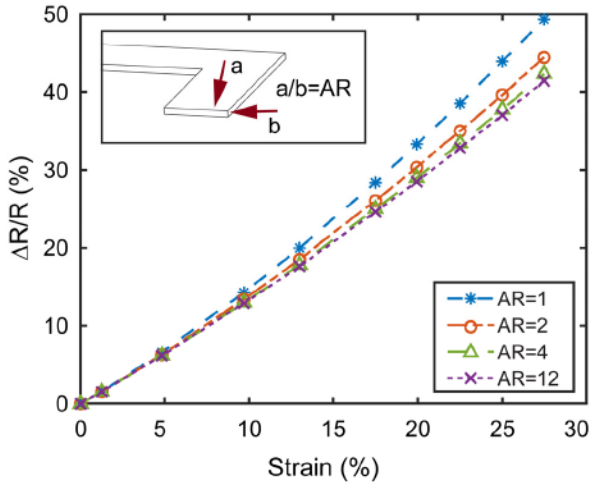

Fig. 9. Effect of aspect ratio (AR) of the embedded micro-channel on the sensitivity of the strain sensor.

Results demonstrate that there is an inverse relationship between the AR and the performance of the sensor. That is, the sensitivity of the strain sensor degrades as the AR ratio increases. For instance, the change in electric resistance, $\Delta R/R$, at 28% strain level is increased by 10% when the aspect ratio decreased from AR = 12 to AR = 1. This implies that square cross-sectional shape, AR = 1, exhibits the maximum sensitivity compared to the other aspect ratios. Generally, when the sensor is under strain, its cross-section shrinks. However, for a channel with smaller AR, the distance between the channel edge and the substrate wall is smaller and consequently causes more shrinkage in the cross-section.

3) Microchannel Cross-Sectional Geometry: Next, the effect of the cross-sectional shape of the embedded channel on the sensitivity of the sensor is investigated. Fig. 10 presents model simulations performed on strain sensors with triangular, square, hexagonal, and octagonal cross-sectional shapes. As shown in Fig. 10, there is an inverse relationship between the number of sides in a given cross-sectional shape and the sensitivity of the strain sensor. For example, a sensor with triangular embedded channels exhibits the highest performance compared to square, hexagonal, and octagonal cross-sectional shapes. This behavior can be explained in light of model

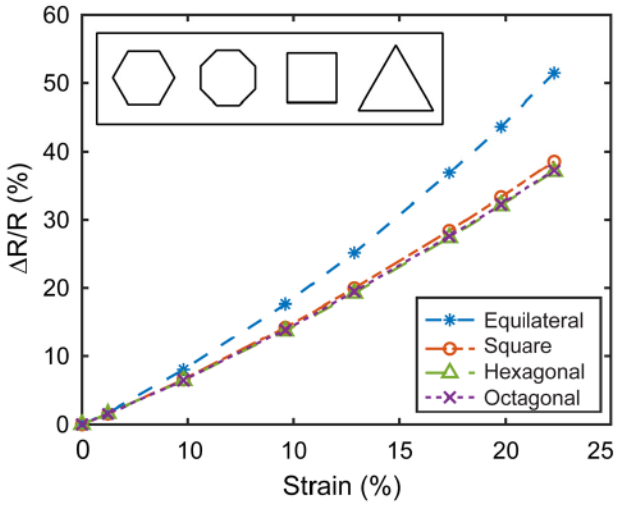

Fig. 10. Effect of the cross-sectional shape of the embedded channels on the sensitivity of the strain sensor while keeping total volume fixed.

animation of the deformed channels when subject to a loading force (See **supplementary material**). Based on these simulations, one can notice that the channel with a triangular cross-sectional shape experiences the highest distortion in the sensor under the uniaxial loading force, while the one with octagonal cross-sectional shows the minimum distortion. This behavior can be explained through the inner angles of the sides. In the triangle cross-section channels, the inner angles are acute compared to the other cross-sectional shapes (square, hexagonal, and octagonal). Thus, there is a higher chance that any deflection will lead to blocking the angles and, therefore, reducing the effective cross-sectional area to conduct the electric charges. Consequently, this turns into higher desirable electric resistance change (ΔR) in the strain sensor. The higher change in resistance leads to higher sensitivity. On the other hand, this behavior is based on the assumption that the areas of all cross-section patterns are the same, therefore, the one with lower edge number experiences more deformation due to proximity to the edge of the substrate.

4) Microchannel Pattern: Fig. 11 compares three common sensor patterns widely reported in the literature. These are spiral (S) [19], [26], vertical serpentine (V) [19], [25], [34], and horizontal serpentine (H) [19] patterns. Results suggest that the sensitivity of the sensor may exhibit positive or negative slopes for different patterns.

In the vertical and spiral patterns, the slope of the strain-sensitivity curve is positive, while the horizontal pattern exhibits a negative slope. This behavior is in agreement with the experimental measurement reported by Park *et al.* [19], as shown in Fig. 11-b. This behavior can be explained in light of the simplified formulation used for describing the change in resistance, ΔR, in relation to the short and long channel sides of the horizontal and vertical patterns. This formulation is based on the linear material assumption, and treats the short and long channels independently, given by:

$$\Delta R_{total} = \Delta R_h + \Delta R_v \tag{12}$$

$$\Delta R_{total} = \rho \frac{L_v}{W_v H_v} \left(\frac{\varepsilon(8-\varepsilon)}{(2-\varepsilon)^2} \right) + \rho \frac{L_h}{W_h H_h} \left(\frac{-\varepsilon}{1+\varepsilon} \right) \tag{13}$$

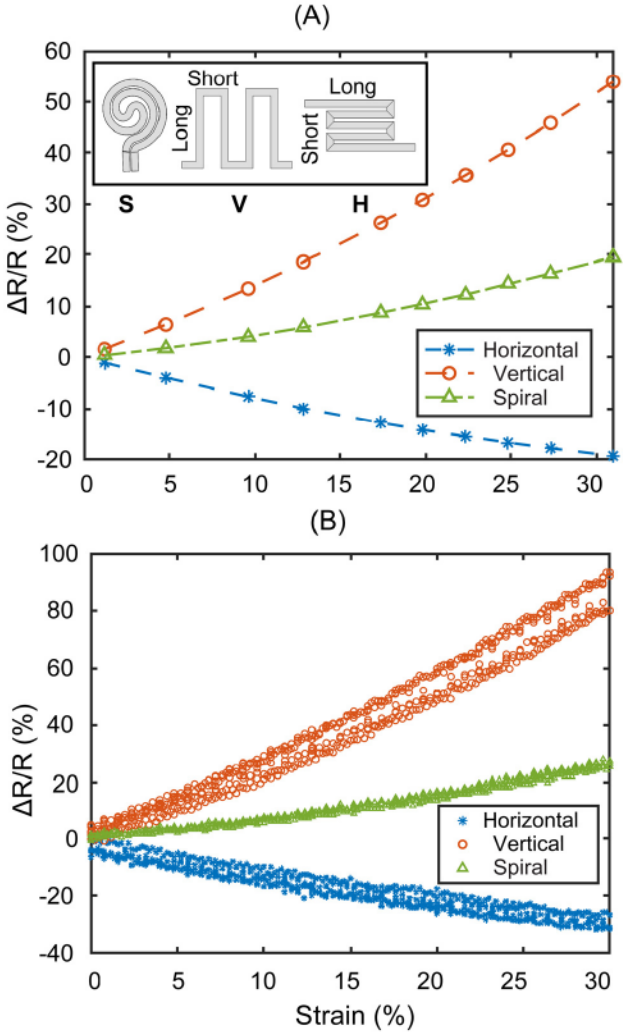

Fig. 11. Comparison of the effect of commonly used patterns of embedded micro-channels (horizontal, vertical and spiral patterns) on the sensitivity of the strain sensor. a) simulation results (this work) b) experimental study from Park *et al* [19].

where ΔR_{total}, ΔR_v, L_v, W_v, and H_v represent the total resistance change, the resistance change of vertical sections of the channel, length of vertical sections of the channel, width of vertical sections of the channel, and height of vertical sections of the channel, respectively. The same notation is used for horizontal sections of the channel. In the vertical pattern, the first and second terms in Eq. (13) are positive and negative, respectively. This is because $L_v \gg L_h$, thus, the contribution of long channels (in determining the sign of the resistance change) is dominant. Consequently, in the vertical pattern, stretching the sensor leads to an increase in the total resistance, ΔR_{total}. On the other hand, the second term in Eq. (13) has a larger impact on resistance change in the horizontal pattern, i.e. $L_h \gg L_v$. Therefore, it causes the sensitivity of the sensor to decline when the strain level increases.

Consequently, as shown in Fig. 11, the slopes are positive and negative for vertical and horizontal configurations, respectively. The same analogy can be made for the spiral pattern. However, the spiral pattern is more complicated due to the lack of simple vertical and horizontal channel patterns. Nonetheless, through mapping the polar design of the spiral pattern

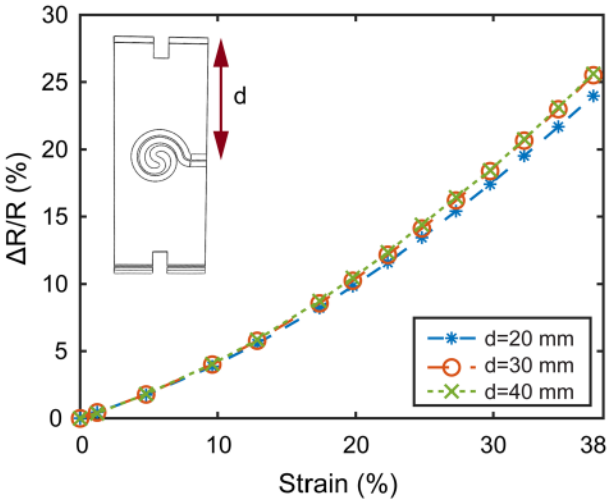

Fig. 12. Effect of vertical location, d, of the embedded micro-channel on sensitivity of the strain sensor. Total length of the substrate is 80 mm.

into horizontal and vertical directions, it can be concluded that $L_{\text{long}} \approx L_{\text{short}}$. Therefore, it is intuitive to conclude that spiral pattern performance falls between the vertical and horizontal patterns (as shown in Fig. 11). The difference between the results reported by Park *et al.* [19] and this work can be ascribed to the difference in sensor's number of loops which also affects the volume of the filled liquid metal in the channel. However, both graphs show the similar behavior for each set of the channel arrangements.

5) Microchannel Position: The location of the embedded channel with respect to the top side of the substrate is studied next. Model simulations were performed only on the spiral pattern because it was the only pattern with enough space for vertical displacement, marked as "d" in Fig. 12. Results in Fig. 12 show that the sensitivity of the sensor is marginally affected by the location of the micro-channel. For example, results presented in Fig. 12 suggest that the sensitivity of the sensor is at its peak when the location of the micro-channel shifts to the center of the substrate. The sensitivity of the sensor declines slightly as the micro-channel location shifts to the top or bottom edges of the sensor.

6) Substrate Material: In the literature, variety of materials have been reported for manufacturing these stretchable strain sensors. Here, three common materials for the substrate are investigated, and results are shown in Fig. 13. These materials are PDMS [19], [26], EcoFlex [25], and NinjaFlex [16]. The material model used for the PDMS is based on the three-parameter Mooney-Rivlin model proposed by Kim *et al.* [34] for the base polymer curing agent ratio of 15:1. Also, the EcoFlex material was simulated using the Neo-Hookean model proposed by Overvelde *et al.* [25]. The strain-stress curves of these three materials are presented in Fig. 13.

By examining Fig. 13, one can notice that NinjaFlex material requires a higher external force to be stretched to the same stretch level as the other two materials. Fig. 14 compares the sensitivity results of the aforementioned materials. Referring to Fig. 14, NinjaFlex shows slightly higher sensitivity, compared to PDMS and EcoFlex, especially at higher strain levels. For example, at a 35% strain level, a sensor with

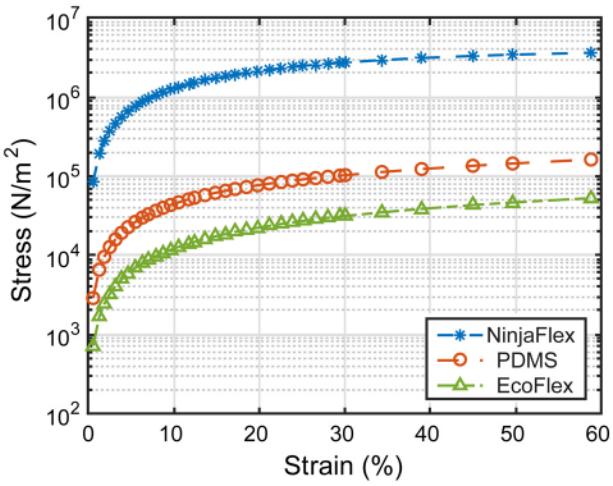

Fig. 13. Comparison between stress-strain curves for the three selected substrate materials obtained using model simulations.

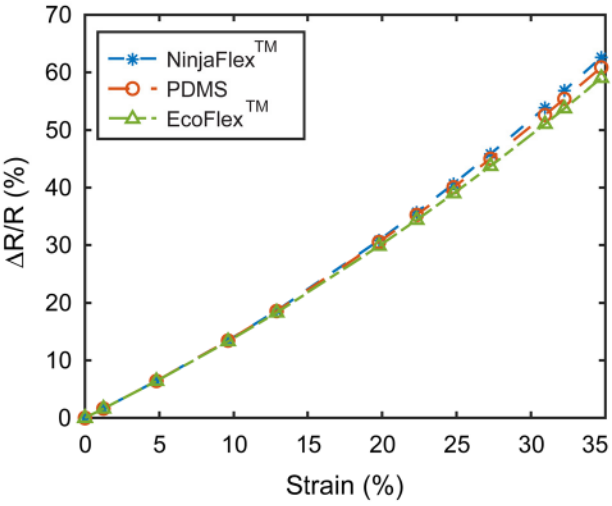

Fig. 14. Effect of traditionally used substrate materials for fabricating strain sensors (PDMS, EcoFlex, and NinjaFlex) on the sensitivity of the strain sensor.

NinjaFlex substrate exhibits, approximately, 6% improvement compared to a sensor with EcoFlex substrate. The order of sensitivity coincides with their stress-stretch order presented in Fig. 13. These results are in good agreement with the data reported by Case [22]. Thus, the use of NinjaFelx as a substrate for a strain sensor is preferred not only because it exhibits a higher sensitivity but, also, because of its adaptability with current FDM 3D printing technologies and the ability to produce intricate designs and three-dimensional complex structures for stretchable sensors.

IV. Conclusion

The rise of rubber-like 3D printing filaments and innovative additive manufacturing techniques has opened the gate for fabricating flexible strain sensors with complex designs and structures. Chief among these strain sensors is the resistive-type strain sensor, which uses a flexible substrate coupled with an electric liquid metal conductor to allow for a change in electric resistance as a result of mechanical deformation in the flexible substrate. The full characterization of these electromechanical systems requires not only understanding

the mechanical response of the sensor but also the electrical response and the coupled electromechanical behavior. To date, simplified analytical formulas have been used to establish a relationship between the electric domain, i.e., change in electric resistance, and mechanical domain, i.e., stress and strain. Moreover, due to the rise of rubber-like substrates, typically used in these sensors, nonlinear models are needed to capture the response of the sensor over a wide range of strain levels.

In this article, a prototype of a resistive-type strain sensor has been fabricated. A finite element COMSOL nonlinear model has been developed and used to characterize the strain sensor as well as established useful design strategies to improve the sensor's response. The strain sensor has been prototyped using the 3D-Printing FDM technique and used for model validation. The fabricated sensor has been characterized experimentally, and results show excellent agreement between model simulations and measured data. Unlike traditionally used linear models, the nonlinear model developed in this work can accurately predict the response of the sensor over a wide range of strain levels because of the nonlinear hyper-elastic model that is coupled with the electrical-mechanical solver. Results from the current study concluded the following:

- The response of the sensor improves as the thickness of the substrate decreases. At a 38% strain level, the sensitivity is increased by 7% when the thickness of the sensor decreased from t = 1.4 mm to t = 0.6 mm.
- The sensitivity of the strain sensor decreases as the aspect ratio of the cross-section of the embedded channel increases. The change in electric resistance at 28% strain level is increased by 10% when the aspect ratio decreased from 12 to 1. This change implies that square cross-sectional shape, i.e., unity aspect ratio, exhibits the maximum sensitivity compared to other rectangular channels with different aspect ratios.
- There is an inverse relationship between the number of sides in a given cross-sectional shape and the sensitivity of the strain sensor. A sensor with triangular embedded channels exhibits the highest performance compared to square, hexagonal, and octagonal cross-sectional shapes (For example,for a fixed strain level of 22%, the change in electric resistances, $\Delta R/R$, of triangular and octagonal cross-sections are 51% and 37%, respectively). The channel with a triangular cross-sectional shape experiences the highest distortion under uniaxial loading force. This results in a larger change in electric resistance and, therefore, higher sensitivity.
- Three commonly used materials for fabricating strain sensors are investigated, including PDMS, EcoFlex, and NinjaFlex. NinjaFlex shows slightly higher sensitivity at higher strain levels. Compared to the PDMS substrate, the use of NinjaFlex filaments is advantageous due to its adaptability with additive manufacturing. Additive manufacturing provides a cost-effective, efficient, and highly versatile approach to fabricating flexible strain sensors. Compared to traditional approaches, such as micro-manufacturing, additive manufacturing allows for the construction of complex designs with limited labor work and no need for special environments.

The nonlinear numerical platform we presented in this article provides full insight into the effects of various design parameters and can serve as a platform for successful design strategies for building flexible strain sensors.

Declaration of Interests

The authors declare that they have no known competing financial interests or personal relationships that could have appeared to influence the work reported in this paper.

References

[1] N. Lu and S. Yang, "Mechanics for stretchable sensors," *Current Opinion Solid State Mater. Sci.*, vol. 19, no. 3, pp. 149–159, 2015.

[2] M. Amjadi, K.-U. Kyung, I. Park, and M. Sitti, "Stretchable, skin-mountable, and wearable strain sensors and their potential applications: A review," *Adv. Funct. Mater.*, vol. 26, no. 11, pp. 1678–1698, Mar. 2016.

[3] J. Lee *et al.*, "A stretchable strain sensor based on a metal nanoparticle thin film for human motion detection," *Nanoscale*, vol. 6, no. 20, pp. 11932–11939, 2014.

[4] J. T. Muth *et al.*, "3D printing: Embedded 3D printing of strain sensors within highly stretchable elastomers (Adv. Mater. 36/2014)," *Adv. Mater.*, vol. 26, no. 36, p. 6202, 2014.

[5] D. M. Vogt, Y.-L. Park, and R. J. Wood, "Design and characterization of a soft multi-axis force sensor using embedded microfluidic channels," *IEEE Sensors J.*, vol. 13, no. 10, pp. 4056–4064, Oct. 2013.

[6] D. Rus and M. T. Tolley, "Design, fabrication and control of soft robots," *Nature*, vol. 521, no. 7553, pp. 467–475, May 2015.

[7] T. Q. Trung and N.-E. Lee, "Flexible and stretchable physical sensor integrated platforms for wearable human-activity monitoringand personal healthcare," *Adv. Mater.*, vol. 28, no. 22, pp. 4338–4372, Jun. 2016.

[8] M. Wehner *et al.*, "An integrated design and fabrication strategy for entirely soft, autonomous robots," *Nature*, vol. 536, no. 7617, pp. 451–455, Aug. 2016.

[9] X. Wang, L. Dong, H. Zhang, R. Yu, C. Pan, and Z. L. Wang, "Recent progress in electronic skin," *Adv. Sci.*, vol. 2, no. 10, Oct. 2015, Art. no. 1500169.

[10] S. Agarwala *et al.*, "Development of bendable strain sensor with embedded microchannels using 3D printing," *Sens. Actuators A, Phys.*, vol. 263, pp. 593–599, Aug. 2017.

[11] V. Correia, C. Caparros, C. Casellas, L. Francesch, J. G. Rocha, and S. Lanceros-Mendez, "Development of inkjet printed strain sensors," *Smart Mater. Struct.*, vol. 22, no. 10, Oct. 2013, Art. no. 105028.

[12] D. R. Myers and A. P. Pisano, "Torque measurements of an automotive halfshaft utilizing a MEMS resonant strain gauge," in *Proc. Int. Solid-State Sens., Actuators Microsyst. Conf. (TRANSDUCERS)*, Jun. 2009, pp. 1726–1729.

[13] R. Zeiser, T. Fellner, and J. Wilde, "Capacitive strain gauges on flexible polymer substrates for wireless, intelligent systems," *J. Sensors Sensor Syst.*, vol. 3, no. 1, pp. 77–86, Apr. 2014.

[14] G. Y. Yang, V. J. Bailey, G. Lin, W. C. Tang, and J. H. Keyak, "Design of microfabricated strain gauge array to monitor bone deformation *in vitro* and *in vivo*," in *Proc. 4th IEEE Symp. Bioinf. Bioeng.*, May 2004, pp. 30–37.

[15] W. Y. Arevalo, C. C. Castiblanco, and C. E. T. Villamizar, "Design and simulation of strain gauge of 3 meanders, for the reduction of external factors," in *Proc. Congreso Internacional de Innovación y Tendencias en Ingenieria (CONIITI)*, Oct. 2019, pp. 1–5.

[16] A. Smith, S. M. Mofidian, and H. Bardaweel, "Three-dimensional printed embedded channel–based resistive strain sensor: Fabrication and experimental characterization," *J. Intell. Mater. Syst. Struct.*, vol. 30, no. 10, pp. 1518–1526, Jun. 2019.

[17] M. Maurizi *et al.*, "Dynamic measurements using FDM 3D-printed embedded strain sensors," *Sensors*, vol. 19, no. 12, p. 2661, Jun. 2019.

[18] N. Lu, C. Lu, S. Yang, and J. Rogers, "Highly sensitive skin-mountable strain gauges based entirely on elastomers," *Adv. Funct. Mater.*, vol. 22, no. 19, pp. 4044–4050, Oct. 2012.

[19] Y.-L. Park, B.-R. Chen, and R. J. Wood, "Design and fabrication of soft artificial skin using embedded microchannels and liquid conductors," *IEEE Sensors J.*, vol. 12, no. 8, pp. 2711–2718, Aug. 2012.

[20] C.-X. Liu and J.-W. Choi, "Patterning conductive PDMS nanocomposite in an elastomer using microcontact printing," *J. Micromech. Microeng.*, vol. 19, no. 8, Aug. 2009, Art. no. 085019.
[21] A. Tabatabai, A. Fassler, C. Usiak, and C. Majidi, "Liquid-phase Gallium–Indium alloy electronics with microcontact printing," *Langmuir*, vol. 29, no. 20, pp. 6194–6200, May 2013.
[22] J. C. Case, E. L. White, and R. K. Kramer, "Soft material characterization for robotic applications," *Soft Robot.*, vol. 2, no. 2, pp. 80–87, Jun. 2015.
[23] H. W. Tan, T. Tran, and C. K. Chua, "A review of printed passive electronic components through fully additive manufacturing methods," *Virtual Phys. Prototyping*, vol. 11, no. 4, pp. 271–288, Oct. 2016.
[24] S. Agarwala, G. L. Goh, and W. Y. Yeong, "Aerosol jet printed strain sensor: Simulation studies analyzing the effect of dimension and design on performance (September 2018)," *IEEE Access*, vol. 6, pp. 63080–63086, 2018.
[25] J. T. B. Overvelde *et al.*, "Mechanical and electrical numerical analysis of soft liquid-embedded deformation sensors analysis," *Extreme Mech. Lett.*, vol. 1, pp. 42–46, Dec. 2014.
[26] Y. R. Jeong *et al.*, "A skin-attachable, stretchable integrated system based on liquid GaInSn for wireless human motion monitoring with multi-site sensing capabilities," *NPG Asia Mater.*, vol. 9, no. 10, p. e443, Oct. 2017.
[27] W. K. Schomburg, Z. Rummler, P. Shao, K. Wulff, and L. Xie, "The design of metal strain gauges on diaphragms," *J. Micromech. Microeng.*, vol. 14, no. 7, pp. 1101–1108, Jul. 2004.
[28] T. Sussman and K.-J. Bathe, "A finite element formulation for nonlinear incompressible elastic and inelastic analysis," *Comput. Struct.*, vol. 26, nos. 1–2, pp. 357–409, Jan. 1987.
[29] A. Rühl, "Introduction," in *On the Time and Temperature Dependent Behaviour of Laminated Amorphous Polymers Subjected to Low-Velocity Impact*. Berlin, Germany: Springer, 2017, pp. 1–8.
[30] H. J. Qi and M. C. Boyce, "Stress–strain behavior of thermoplastic polyurethanes," *Mech. Mater.*, vol. 37, no. 8, pp. 817–839, Aug. 2005.
[31] T. Reppel and K. Weinberg, "Experimental determination of elastic and rupture properties of printed ninjaflex," *Technische Mechanik. Sci. J. Fundam. Appl. Eng. Mech.*, vol. 38, no. 1, pp. 104–112, 2018.
[32] G. Marckmann and E. Verron, "Comparison of hyperelastic models for rubber-like materials," *Rubber Chem. Technol.*, vol. 79, no. 5, pp. 835–858, Nov. 2006.
[33] C. Karcher, V. V. Kocourek, and D. Schulze, "Experimental investigations of electromagnetic instabilities of free surfaces in a liquid metal drop," in *Proc. Int. Sci. Colloq., Modelling Electromagn. Process.*, 2003, pp. 105–110.
[34] T. K. Kim, J. K. Kim, and O. C. Jeong, "Measurement of nonlinear mechanical properties of PDMS elastomer," *Microelectron. Eng.*, vol. 88, no. 8, pp. 1982–1985, Aug. 2011.

S. M. Mahdi Mofidian received the B.Sc. degree from the University of Tehran, the M.Sc. degree from the Iran University of Science and Technology, and the Ph.D. degree in micro/nano engineering from Louisiana Tech University in 2019. He is currently an Adjunct Faculty with the Mechanical Engineering Department, Louisiana Tech University. His current research interests include the design and analysis of nonlinear vibration devices, energy harvesting, sensors and actuators, and computational fluid dynamics.

Shayan Davani received the Ph.D. degree in engineering (micro/nano scale systems) from Louisiana Tech University, Ruston, LA, USA, in 2019. He is currently a Postdoctoral Fellow Researcher with Louisiana Tech University. He has conducted research in design, fabrication, and the simulation of MEMS and microfluidics. His current research interest includes the investigation of effective pool boiling heat transfer surfaces.

Kasra Momeni received the B.Sc. degree in multiscale modeling of carbon nanotube reinforced nanocomposites from KNT University in 2005, the M.Sc. degree in mechanical engineering from the Sharif University of Technology in 2008 for developing a novel multiscale modeling scheme based on artificial intelligence, and the Ph.D. degree from the Aerospace Engineering Department, Iowa State University, in 2015, with a focus on theoretical and computational approaches to phase transforming materials. From 2015 to 2020, he was an Assistant Professor of Mechanical Engineering at Louisiana Tech University. He is currently an Associate Professor of Mechanical Engineering with the University of Alabama. Dr. Momeni received the Aeroscape Engineering Fellowship in 2014, both Iowa State University's Research and Teaching Excellence Awards in 2015, the Zaffarano Prize Honorable Mention Award for 2015, the National Recognition Award of Louisiana Tech University in 2019, and the National Science Foundation CAREER Award in 2020.

Hamzeh Bardaweel received the M.Sc. and Ph.D. degrees in mechanical engineering from Washington State University, in 2007 and 2010, respectively. Prior to joining Louisiana Tech, he worked as a Postdoctoral Fellow with the University of California, Davis, and Clemson University, in 2010 and 2015, respectively. Since September 2015, he has been an Assistant Professor of Mechanical Engineering with Louisiana Tech University and managed his own externally funded Research Group. His current research interests include design, analysis, and fabrication of smart structures and systems including vibration energy harvesting systems and self-powered sensors.